

Angular scattering of sound from solid particles in turbulent suspension

Stephanie A. Moore and Alex E. Hay

Department of Oceanography, Dalhousie University, Halifax, Nova Scotia B3H 4J1, Canada

(Received 9 October 2008; revised 6 June 2009; accepted 25 June 2009)

Sound scattering by solid particles suspended in a turbulent jet is investigated. Measurements of the scattered amplitude were made in a bistatic geometry at frequencies between 1.5 and 4.0 MHz, and at scattering angles from 95° to 165° relative to the forward direction. Two types of particle were used: nearly spherical lead-glass beads and aspherical natural sand grains. For each particle type, experiments were carried out using ~ 200 and $\sim 500 \mu\text{m}$ median diameter grain sizes, corresponding to $0.7 \leq ka \leq 4$. The sphericity of the sand grains, defined as the ratio of projected perimeter size to projected area size, was 1.08. The lead-glass bead results are consistent with an elastic sphere model. A rigid movable sphere model provides the best fit to the sand data, and the best-fit diameter is within 4% of the equivalent volume size. However, the scattering pattern for sand is systematically smoother than predicted: that is, the undulations in the angular scattering pattern predicted by spherical scatterer theory are present, but muted. This observed departure from spherical scatterer theory is attributed to disruption of the interference among creeping waves by the irregular surfaces of natural sand grains.

© 2009 Acoustical Society of America. [DOI: 10.1121/1.3180696]

PACS number(s): 43.30.Ft, 43.20.Fn [KGF]

Pages: 1046–1056

I. INTRODUCTION

Acoustic remote sensing systems are becoming a primary tool for sediment dynamics research and sediment transport monitoring in aqueous environments (see Ref. 1 for a recent review). The sound scattered from particles in suspension can provide information on their velocity, size, and concentration and thus, importantly, on the sediment flux. Inverse methods for extracting the size and concentration estimates, however, are dependent on a suitably accurate representation of the scattering cross section which, for randomly-oriented assemblages of irregularly shaped particles, is not readily amenable to calculation from first principles. Thus, in the interpretation of scattering measurements from suspensions of natural sand, the grains are assumed to be spherical on average.

Previous experimental investigations have shown that a modified spherical scatterer model can be used to represent the total scattering and backscattering cross sections of suspensions of natural sand.^{2–4} These results provide an adequate basis for the inverse problem in dilute suspensions, for which multiple scattering is unimportant. At concentrations exceeding approximately 1% by volume, however, multiple scattering effects cannot be ignored.⁵ Such concentrations are encountered in close proximity to the bed, and become especially important in high energy (i.e., sheet flow) conditions.⁶ Theoretical estimates of the effects of multiple scattering on the detected signal necessarily require knowledge of the dependence of single particle scattered energy on scattering angle. However, no experimental evidence exists to support the use of a spherical scatterer model at scattering angles other than 0° and 180° .

This paper presents measurements of the variation with scattering angle of the differential scattering cross section of

solid particles in aqueous suspensions as a function of acoustic frequency and mean grain size. Both natural sand grains and manufactured lead-glass beads are used in the experiments. The observed cross sections are compared to predictions based on spherical scatterer theory. The primary goals of the paper are to determine the following: (1) whether a spherical scatterer model provides a good fit to the angular variation of sound scattered from irregularly shaped particles like sand, (2) whether an elastic or a rigid sphere model provides the better fit, and (3) whether the experiments provide physical grounds for seeking improvements to the spherical scatterer approximation for natural sand grains.

The measurements were made for values of $0.7 \leq ka \leq 4$ (k being the acoustic wavenumber, a the scatterer radius). This ka range is typical of acoustic remote sensing studies of sand transport dynamics. As the lowest frequency resonance for a quartz-like or glass-like sphere in water occurs at $ka \sim 5.5$,⁷ resonance scattering should be relatively unimportant for $ka < 4$. It is expected therefore that variations in scattered energy with scattering angle over the ka range of the present measurements should be mainly due to the effects of diffraction. Thus, the focus here is on $O(1)$ values of ka , and the effects of the irregular shapes of natural sand grains on diffraction-induced features in the differential scattering cross section.

II. THEORY

Since the waves scattered from individual particles embedded in turbulence add incoherently on average, the average scattered intensity is proportional to the particle number density, N . The ensemble mean-square scattered pressure, $\langle p_s^2 \rangle$, can then be written as (Ref. 8, pp. 438–441)

$$\langle p_s^2(\theta) \rangle = \frac{p_i^2}{r^2} \exp \left[-2\alpha_0 r + \int_0^r N(r) \Sigma_s dr \right] \int_V N \sigma_s(\theta) dV, \quad (1)$$

where $\langle \rangle$ denotes the ensemble average, p_i the incident pressure amplitude, α_0 the attenuation in water, Σ_s the total scattering cross section, σ_s the differential scattering cross section, and θ the scattering angle. V is the detected volume, assumed here to have characteristic dimensions small compared to r , the radial distance from V to the receive transducer. As we are considering solid scatterers, it has been assumed that the absorption cross section of the particles can be ignored relative to Σ_s . Note also that Eq. (1) applies to the low scatterer concentrations for which multiple scattering is unimportant.

Assuming that the detected volume changes very little with scattering angle, and that $\sigma_s(\theta)$ is constant within V (the validity of these assumptions is examined in Appendix A), then the ratio of the mean-square pressures at a given scattering angle, θ_0 , and at a reference scattering angle, θ_r , is

$$\frac{\langle p_s^2(\theta_0) \rangle}{\langle p_s^2(\theta_r) \rangle} = \frac{\sigma_s(\theta_0)}{\sigma_s(\theta_r)}. \quad (2)$$

The dependencies on incident pressure, particle concentration, and attenuation along the scattered path are thus eliminated. Equation (2) provides the basis for the comparisons between theory and experiment which are presented later in this paper: the measurements yield the ratio on the left; theory that on the right.

Ignoring thermal and viscous effects, the scattered pressure, p_s , for a plane-wave incident on a solid elastic sphere can be written as a sum of partial scattered waves⁹ (p. 273):

$$p_s = \frac{|p_i|}{kr} \sum_{n=0}^{\infty} (2n+1) i^{n+1} \sin \eta_n e^{-i\eta_n} P_n(\cos \theta) e^{i(kr - \omega t)}, \quad (3)$$

where ω is the angular frequency, t is time, P_n is the Legendre polynomial of order n , and η_n is the phase shift of the n th partial wave.¹⁰ The amplitude of the scattered wave can also be written in terms of the far-field form factor, f_∞ , as

$$|p_s| = \frac{|p_i| |f_\infty| a}{2r}, \quad (4)$$

where f_∞ is given by

$$f_\infty = \frac{2}{ka} \sum_{n=0}^{\infty} (2n+1) i^{n+1} \sin \eta_n e^{-i\eta_n} P_n(\cos \theta). \quad (5)$$

Thus the differential scattering cross section, which is the ratio of scattered power to incident intensity⁸ (p. 426), is

$$\sigma_s = \frac{|f_\infty|^2 a^2}{4}. \quad (6)$$

The elastic properties of the scatterer enter the computations through the phase shift. The expressions for the phase shift used here are based on Eq. (30) in Ref. 10. Other than scatterer size and the incident wave frequency, the physical properties upon which the resulting phase shifts explicitly depend

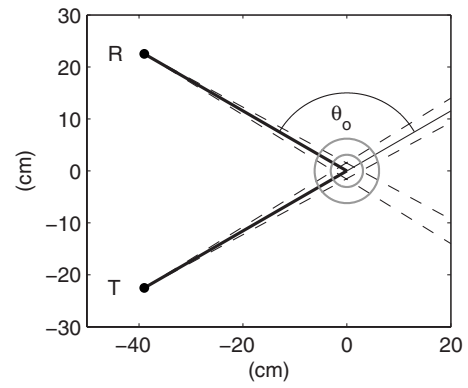


FIG. 1. Scale diagram of the scattering geometry in plan view. The jet axis is into the page, and the jet location is indicated by the concentric grey circles centered at the origin, with radii of σ_j and $2\sigma_j$, respectively, where σ_j is the standard deviation of the sediment concentration profile transverse to the jet axis. T and R represent the transmit and receive transducers, and the heavy black lines indicate the incident and scattered rays for a particle at the jet centreline. The scattering angle for a particle at the centerline, θ_0 , is also shown and has a value of 120° in the diagram. The dashed lines represent $\pm 5\beta_0$ (i.e., five times the transducer half-power beamwidth) at 2.9 MHz, to illustrate the narrowness of the beams relative to the width of the jet.

are the densities of, and compression wave speeds in, the fluid medium and the solid scatterer, and the shear wave speed in the scatterer.^{10,11} Thus, an error pointed out by Hickling¹² (see also Ref. 13) involving Poisson's ratio does not enter the computations. The relevant parameter values used here are $\rho=2650$ kg/m³, $c_p=5100$ m/s, and $c_s=3200$ m/s for quartz;⁷ $\rho=2870$ kg/m³, $c_p=4870$ m/s, and $c_s=2930$ for lead-glass;¹⁴ and $\rho=998$ kg/m³, $c_p=1483$ m/s for water.¹⁵ The quartz values are used for the comparisons of the theory with the measurements for sand. For the rigid movable sphere case, the shear modulus is infinite, and computations were made using the expressions for the phase shifts in this limit.^{7,10}

III. METHODS

A. Scattering

The jet tank facility in which the measurements were made is a slightly modified version of that described previously.¹⁶ A vertically-oriented turbulent jet and recirculation system maintain a suspension of particles with a quasi-steady mean concentration, except for a small ($< 15\%$) decrease with time over the course of an ~ 40 min duration experiment (see below). Since the particles are spatially confined within the jet, it is possible to carry out far-field scattering experiments in a crossed-beam geometry without having to correct for attenuation due to particles along the incident and scattered paths (Fig. 1). The modifications to the facility involved: (a) adding a speed controller to the sediment circulation pump and (b) adding an insert to the discharge orifice, thereby reducing the nozzle diameter. As a result of the latter modification, the region of the jet in which the scattering measurements were made was located at a greater distance (measured in nozzle diameters) from the point of discharge.

The suspension is discharged from a 0.95 cm diameter circular nozzle, and recirculated by a variable-speed centrifugal

gal pump. Two broadband transducers were positioned 52.8 cm below the nozzle and 45 cm from the jet centerline. Particle concentrations at this height were determined gravimetrically from samples drawn by suction from the jet axis. Centerline concentrations ranged from ~ 1 to ~ 6 kg/m³. These concentrations are low enough (i.e., $<0.3\%$ by volume) that multiple scattering should have been negligible. Prior to the experiments, the water in the tank had been aged for several months to avoid contamination of the signal by scattering from microbubbles. The absence of bubbles was confirmed by checking that no detectable signal was received from the range interval spanning the jet prior to the addition of particles. To prevent any buildup of algae or dust within the tank, the water was continuously filtered through a 1 μ m pore-size filter, and 200–300 ml of chlorine bleach were added to the water approximately once a month.

To measure the scatterer concentration, 1 L samples were drawn by suction from the jet centerline at the level of the transducers. The samples were filtered (18.5 cm diameter Q8 Fisher brand filters) and oven-dried at 40 °C for 24–48 h. The dry sand was removed from the filter and weighed to 0.1 mg precision using a Mettler AJ100 balance. This procedure was tested by filtering and drying 12 samples with known initial weights of ~ 5 g for 24, 47, 71, and 80 h. Three samples were removed from the oven at each drying time, and the final weights measured. The average difference between initial and final weights was -0.17% , and ranged between -0.08% and -0.23% for the four drying times. No discernable trend with drying time was observed.

Three suction samples were drawn at the start and end of each scattering experiment. Suspended sediment concentration, M , was determined from the dry weight of the sand and the volume of water in the sample. The standard deviation of M among the three samples as a percentage of the mean ranged from 0.8% to 12.5%. A second set of triplicate samples was drawn at the end of each experiment, i.e., approximately 40 min after the first set. Scatterer concentrations decreased by 5%–15% over this time interval, because particles inevitably escape from the jet: i.e., the capture cone¹⁶ at the base of the tank is not 100% efficient. The trends with scattering angle associated with this 5%–15% drop in concentration were not removed from the observations.

The broadband piezocomposite transducers (Imasonic) used in this study have a center frequency of 3.0 MHz. Measurements were made between 1.5 and 4.0 MHz at 0.125 MHz intervals: i.e., at 21 separate frequencies. The transmit pulse was produced by a programmable arbitrary waveform generator (National Instruments 5411). The transmit pulse length was 16 μ s, corresponding approximately to a 0.0625 MHz energy bandwidth in the pulse, i.e., half the 0.125 MHz frequency interval between adjacent frequencies, assuring negligible frequency overlap in the data at a given scattering angle. This pulse length also corresponds to 1.2 cm resolution in range, which is much less than the 6 cm characteristic width of the jet (see Fig. 1, and below). Thus, the signal at the range corresponding to the jet centerline is representative of the more uniform mean concentration at that location. The ping interval was 10 ms, long enough for

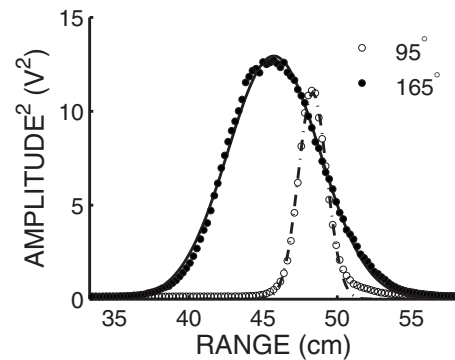


FIG. 2. Squared mean signal amplitude versus range for the large (approximately 500 μ m median grain diameter) sand at scattering angles of 95° and 165°. The lines are the best-fit Gaussians, with standard deviations of 0.96 and 3.10 cm, respectively.

echoes to die out at these frequencies. The receive signal, after amplification and rectification, was digitized at 320 kHz with 12-bit resolution. The signals from 10 pings were ensemble-averaged and stored, and 100 ensemble-averaged profiles were acquired at each frequency and angle.

The transducers were mounted equidistant from the jet centerline in a bistatic configuration with their acoustic axes in the same horizontal plane and intersecting at the jet centerline (Fig. 1). Each transducer was suspended from a rigid arm which could be rotated in the horizontal plane about a pivot point at the jet centerline. Measurements were made at scattering angles from 95° to 165° in 5° increments, starting at 165°. At the end of each experiment, a duplicate set of measurements was collected at 165°. The resulting differences in signal amplitude were typically less than 5%, and non-systematic.¹⁷

The discharge velocity at the nozzle was 4 m/s. Using the nozzle diameter as a length scale, the discharge Reynolds number was $\sim 3 \times 10^4$. The transducer beams intersected the jet at an axial distance from the discharge of 55 nozzle diameters. At this distance, time-averaged transverse profiles of velocity and scalar quantities, including suspended sediment concentration, are expected to be Gaussian for turbulent round jets.^{16,18} The square of the time-averaged scattered signal provides a measure of concentration [Eq. (1)]. Profiles of the squared rms voltage for the large sand grains at $\theta = 95^\circ$ and 165° are shown in Fig. 2, together with the best-fit Gaussians. Designating σ_j as the standard deviation of the Gaussian fit, the characteristic width of the jet, $2\sigma_j$, is 6.2 cm at the 165° scattering angle. As the figure indicates, the profile at 95° is much narrower. This reduction in apparent width is a geometric effect, arising primarily from the reduced overlap of the transmit and receive transducer beam patterns as the scattering angle approaches 90° (see Appendix A). Since the received voltage is proportional to the scattered pressure, the peak value in the rms scattered voltage profiles (i.e., the data, not the fit in Fig. 2) was used for the left-hand side of Eq. (2) in the comparisons between theory and experiment presented later.

As a quantitative measure of how well the various models fitted the data, the χ^2 statistic was computed. (χ^2 is one minus the error variance skill score defined in Ref. 19.) For

observations, X , and predictions, Y , both of which are functions of frequency and scattering angle, this statistic is given by

$$\gamma^2 = \frac{\text{Var}(X - Y)}{\text{Var}(X)}, \quad (7)$$

where Var denotes the variance with respect to the mean over all values in the $[\theta, f]$ domain spanned by the observations. Since this statistic is normalized by the variance of the observations, differences in γ^2 values provide unbiased measures of the relative predictive skill of different models. The theoretical prediction with the smallest value of γ^2 represents the best fit. In addition, the correlation coefficient, R^2 , between the values of X and Y with means removed, and the rms deviation $\epsilon = \sqrt{\text{Var}(X - Y)}$, also with means removed, were computed for each set of observations and corresponding best-fit theory.

B. Particle size

For both the lead-glass beads and sand two sizes were used: one with a median diameter of $\sim 200 \mu\text{m}$ and the other $\sim 500 \mu\text{m}$, referred to hereinafter as the “small” and “large” particles. The sand used was first sieved into narrow (1/4-phi) fractions. (The phi-scale is given by $-\log_2 d$, with d the particle diameter in millimeters.) The sand retained between the 180 and 212 μm sieves is the small sand, while the large sand was that retained between the 425 and 500 μm sieves. High resolution sand size distributions were determined via electroresistance (Coulter Counter) and image analysis using the sand from the suction samples drawn from the jet. The lead-glass beads were ordered from the manufacturer in relatively narrow size distributions. High resolution size distributions for the lead-glass beads were obtained by Coulter Counter using the suction samples taken from the jet. The image analysis methodology could not be applied to these particles because they are transparent.

For the sieve analyses, samples weighing 10–15 g were shaken in a stack of 20 cm diameter sieves for 15 min following accepted procedures.²⁰ National Institute of Standards and Technology (NIST) 1017b and 1018b glass beads were used to calibrate the sieves.

For the Coulter Counter measurements, roughly 0.5 g of particles from the jet suction samples were suspended in a 4 L beaker containing a solution of 64% de-ionized distilled water, 35% glycerine, and 1% sodium chloride. The Coulter Counter (model Multisizer II) was used with a 1000 μm diameter aperture. Between 5000 and 10 000 particles were counted in each run. Two separate runs were averaged for

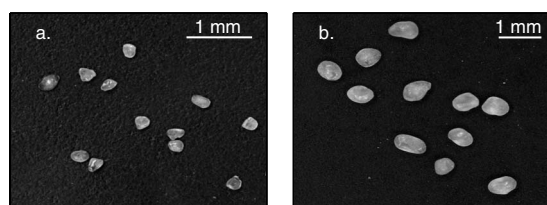


FIG. 3. Photographs of (a) the small and (b) the large sand grains.

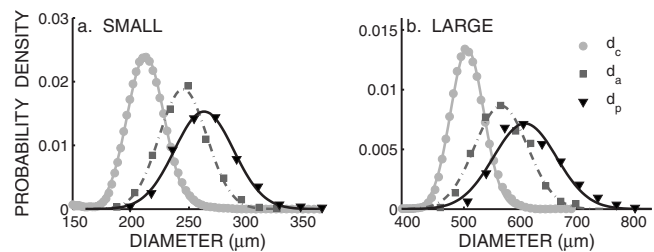


FIG. 4. Size distributions determined by Coulter Counter and image analysis for (a) the small sand (approximately 200 μm median grain diameter) and (b) the large sand (approximately 500 μm median grain diameter). The symbols in the legend indicate the different diameter estimates, as follows: d_c , the Coulter Counter diameter; d_a , diameter based on the projected area; and d_p , diameter based on projected perimeter. The d_a and d_p estimates were determined by image analysis. Points represent data and lines represent the best-fit Gaussian distributions.

each particle type, yielding distributions of the (volume) equivalent spherical diameter.²¹ The Coulter Counter size estimates are designated by d_c .

Size determination by image analysis was based on 3872×2592 pixel photographs of the particles resting on a flat surface taken with a Nikon D80 digital single-lens reflex camera equipped with a 60 mm focal length macro lens. Example images of the small and the large sand grains are shown in Fig. 3. Particle boundaries were determined using an edge detection method based on a pixel brightness threshold. Equivalent diameters corresponding to the equal projected area sphere, d_a , were determined from the area enclosed by each boundary and the equal projected perimeter sphere, d_p , from the perimeter of the enclosed area. The ratio d_p/d_a for each particle, averaged over a large number of particles, is approximately equivalent to averaging over particle orientation. This average, $\langle d_p/d_a \rangle$, provides a measure of particle sphericity. Photographs of nominally spherical (black) basalt beads of comparable size were analyzed using the same approach to validate the method.

The Coulter Counter and image analysis size distributions are used for the comparisons between theory and experiment because (1) being based on the samples drawn from the jet centerline, they are representative of the actual size distributions of the scatterers in the jet, and (2) they resolve the distributions within each 1/4-phi sieve fraction.

IV. RESULTS

A. Particle size

The size distributions for the small and large sand, as measured with the Coulter Counter, are shown in Fig. 4. Both distributions are nearly Gaussian. Table I lists d_{16} , d_{50} ,

TABLE I. Coulter Counter size distribution statistics.

Particle	d_{16} (μm)	d_{50} (μm)	d_{84} (μm)
Small sand	196	211	227
Large sand	476	502	532
Small beads	182	212	242
Large beads	384	424	471

TABLE II. Image analysis size distribution statistics. N is the number of analyzed particles while d and σ are the distribution mean and standard deviation. Subscripts a and p denote parameters from projected area and projected perimeter, respectively.

Particle	N	$d_a \pm \sigma_a$ (μm)	$d_p \pm \sigma_p$ (μm)	$d_p/d_a \pm a$
Small sand	999	245 \pm 21	265 \pm 26	1.08 \pm 0.03
Large sand	582	569 \pm 44	618 \pm 55	1.08 \pm 0.03
Small basalt	442	188 \pm 10	193 \pm 11	1.024 \pm 0.009
Large basalt	176	455 \pm 24	475 \pm 26	1.044 \pm 0.006

and d_{84} for both the sand and the lead-glass beads. These diameters represent to the 16th, 50th, and 84th percentiles of the cumulative distribution, and correspond to the mean and one standard deviation below and above the mean for a Gaussian distribution.

The sand size distributions determined by image analysis are also plotted in Fig. 4, and the statistics summarized in Table II. The average value of d_p/d_a for both sand sizes was 1.08 ± 0.03 . The same analysis for the nominally spherical basalt beads yielded 1.02 ± 0.009 and 1.04 ± 0.006 for the small and large bead sizes, respectively. As a further comparison, averaging over the projections of all possible orientations of a unit cube in a simulation gave $\langle d_p/d_a \rangle \sim 1.4$. The latter value is larger than the 1.08 measurement for sand, indicating that the sand grains used in the experiments were less angular than cubes, consistent with their somewhat rounded appearance (Fig. 3).

As expected for non-spherical particles, the size distributions for sand obtained with the various methods differ noticeably. The ratios of mean Coulter Counter size to mean projected area size, d_c/d_a , are 0.80 for the small sand and 0.84 for the large sand. Some of the difference between these two measures of size can be attributed to biases intrinsic to the different techniques. For comparison, other investigators²² have found that, for a unimodal distribution of 300–500 μm sieve diameter “spherical” and “nearly spherical” standard reference glass beads, the average value of d_c/d_a was 0.86, similar to the values obtained here.

B. Scattering results

The observed and best-fit theoretical angular scattering patterns for the small lead-glass beads and small sand are shown in Fig. 5. The data for lead-glass are the average of three experiments, those for sand the average of two. The corresponding results for the large particles are presented in Fig. 6, the data being the average of three experiments for both particle types. All scattered amplitudes have been normalized by the values at 165° : i.e., in Eq. (2), $\theta_r = 165^\circ$.

The normalized theoretical scattered amplitude, Y , is given by

$$Y = \frac{\sqrt{\int_0^\infty |f_\infty(\theta, a)|^2 a^2 n(a) da}}{\sqrt{\int_0^\infty |f_\infty(165^\circ, a)|^2 a^2 n(a) da}}, \quad (8)$$

where $n(a)$ is the particle size probability density. Y was computed for a range of mean diameters in steps of 10 μm using Gaussian size distributions with the same breadth-to-

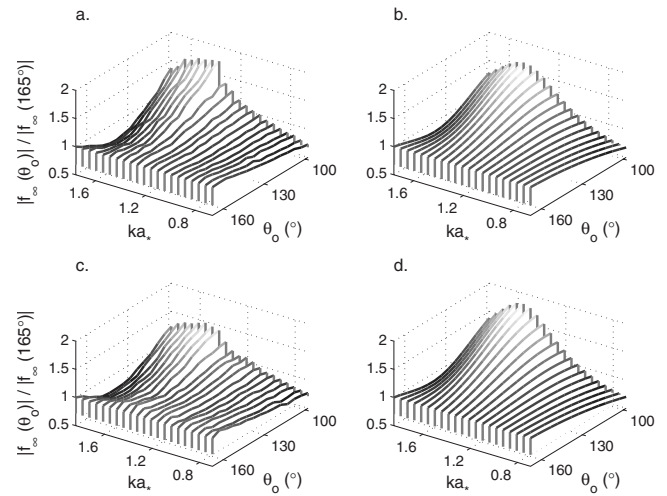


FIG. 5. Observed and predicted angular scattering patterns normalized by the amplitude at $\theta_0 = 165^\circ$ for [(a) and (b)] small lead-glass beads and [(c) and (d)] small sand. Data are on the left, best-fit theory on the right. The theoretical computations assume elastic spheres for the glass beads ($d_* = 2a_* = 210 \mu\text{m}$, $\sigma_* = 30 \mu\text{m}$), and rigid spheres for the sand grains ($d_* = 2a_* = 220 \mu\text{m}$, $\sigma_* = 17 \mu\text{m}$).

mean diameter ratios (i.e., σ/d_{50}) as the Coulter Counter results. For each particle type, the mean diameter and model (rigid or elastic sphere) yielding the minimum value of γ^2 were deemed the best fit.

The γ^2 values corresponding to the best-fit models for the different particle types are plotted in Fig. 7 versus d/d_* , where d is the theoretical mean diameter, and d_* is the best-fit theoretical mean. The minimum values of γ^2 (i.e., the values at $d = d_*$) for the best-fit models in each case are listed in Table III, together with the corresponding values of ϵ and R^2 . In all cases, the best-fit diameter, d_* , is very close to the median Coulter Counter size. The minima in Fig. 7 tend to

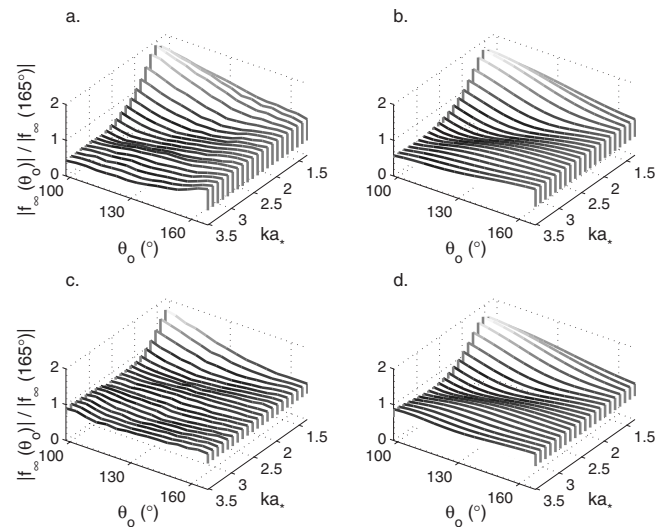


FIG. 6. Observed and predicted angular scattering patterns normalized by the amplitude at $\theta_0 = 165^\circ$ for the large particles: [(a) and (b)] large lead-glass beads; [(c) and (d)] large sand. Data are on the left, and best-fit theory on the right. (Note: the viewpoint is different from Fig. 5.) The theoretical computations assume elastic spheres for the glass beads ($d_* = 2a_* = 420 \mu\text{m}$, $\sigma_* = 44 \mu\text{m}$) and rigid spheres for the sand grains ($d_* = 2a_* = 520 \mu\text{m}$, $\sigma_* = 29 \mu\text{m}$).

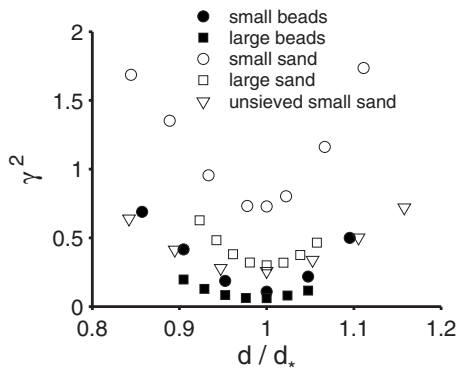


FIG. 7. The values of γ^2 for the best-fit models versus the ratio of theoretical mean diameter, d , to the best-fit theoretical mean diameter, d_* , for all scatterer types.

be more pronounced for the small and large sand, due to their size distributions being relatively narrow compared to those of the lead-glass beads and the unsieved sand (Table III).

Over the measured frequency range, the values of d_* correspond to ka_* ranges of 0.66–1.76 for the small lead-glass beads, and 0.69–1.84 for the small sand. In contrast, the ranges for the large particles are $1.32 \leq ka_* \leq 3.52$ for lead-glass and $1.63 \leq ka_* \leq 4.36$ for sand. For quartz-like and/or glass-like particles, the rigid and elastic sphere model predictions differ by less than 7% for $ka < 1$, whereas for $1 < ka < 4$ they differ by as much as 30%. Thus, the effects of the scatterer elastic constants on the predictions are much greater at the higher ka values corresponding to the larger particles. This is reflected by the greater differences in γ^2 between the two models for the large particles, compared to the corresponding differences for the small particles (Table IV). Consequently, the present results demonstrate that (1) the elastic model provides the better fit to the lead-glass bead data and (2) the rigid model the better fit to the sand data.

For the most part, the observed and predicted surfaces in Figs. 5 and 6 exhibit good qualitative and quantitative agreement. For sand, however, while the overall shapes of the experimental and theoretical scattering patterns are similar, the ridges and valleys in the observed patterns are less pronounced than the predictions. This effect, which is clearest in the results for large sand grains [Figs. 6(c) and 6(d)], contributes to the systematically higher values of γ^2 for sand compared to lead-glass.

The large bead and sand data are plotted versus scattering angle for three frequencies in Fig. 8, together with the predictions from the best-fit rigid and elastic sphere models.

TABLE IV. The values of γ^2 computed for the elastic and rigid sphere models using d_* as the theoretical mean diameter.

Scatterer	d_* (μm)	γ^2 (elastic)	γ^2 (rigid)
Small beads	210	0.11	0.12
Large beads	420	0.06	0.19
Small sand	220	1.01	0.73
Large sand	520	0.71	0.30

Also shown are the predictions of the high-pass model. This model was originally put forward by Johnson²³ for backscatter from a fluid sphere, and later modified for total scattering from sand grains.² The latter study also suggested a form of the high-pass model for angular scattering, but with no supporting observational evidence, as none was available at the time. Figure 8 indicates that the elastic sphere model best reproduces the measured values for the lead-glass beads, whereas the rigid sphere model best reproduces the large sand data. In addition, the results in Fig. 8 demonstrate that the high-pass model does an unacceptable job of reproducing the observations for either scatterer type.

Additional scattering measurements were carried out with unsieved small sand: that is, the small sand before it was sieved into 1/4-phi size fractions. The values of γ^2 from the best-fit theory to the data are plotted versus d/d_* in Fig. 7. The overall best-fit parameters are summarized in Table III. As for the narrow sand fractions, the best-fit model for these sand data is the rigid sphere. The fit yielded a minimum γ^2 value of 0.26, comparable to the 0.30 value for the large sand.

V. DISCUSSION

A. The effects of irregular particle shape: Diffraction smearing

Overall, the best agreement between measured and predicted scattering was obtained for the large lead-glass beads and the elastic sphere model, yielding a minimum value of γ^2 of 0.06 (Table IV). For comparison, the minimum γ^2 value for the large sand and the rigid sphere model was 0.30. It is concluded that, for the ka range of the present measurements, a rigid sphere is not as good a model for scattering by natural sand grains as is the elastic sphere model for the lead-glass beads. The likely cause of this difference is the irregular shape of the sand grains.

TABLE III. Summary statistics for the best-fit models to the angular scattering data. Particle size statistics (from Coulter Counter analysis except for the “unsieved” sand, which are from sieve analysis) are included for convenience.

Scatterer	d_{50} (μm)	$(d_{84}-d_{16})/2$ (μm)	Model	d_* (μm)	ϵ	R^2	γ^2	d_*/d_{50}
Small beads	212	30	elastic	210	0.09	0.95	0.11	0.99
Large beads	424	44	elastic	420	0.10	0.97	0.06	0.99
Small sand	211	16	rigid	220	0.18	0.91	0.73	1.04
Large sand	502	28	rigid	520	0.08	0.92	0.30	1.04
Unsieved sand	203	62	rigid	190	0.08	0.86	0.26	0.94

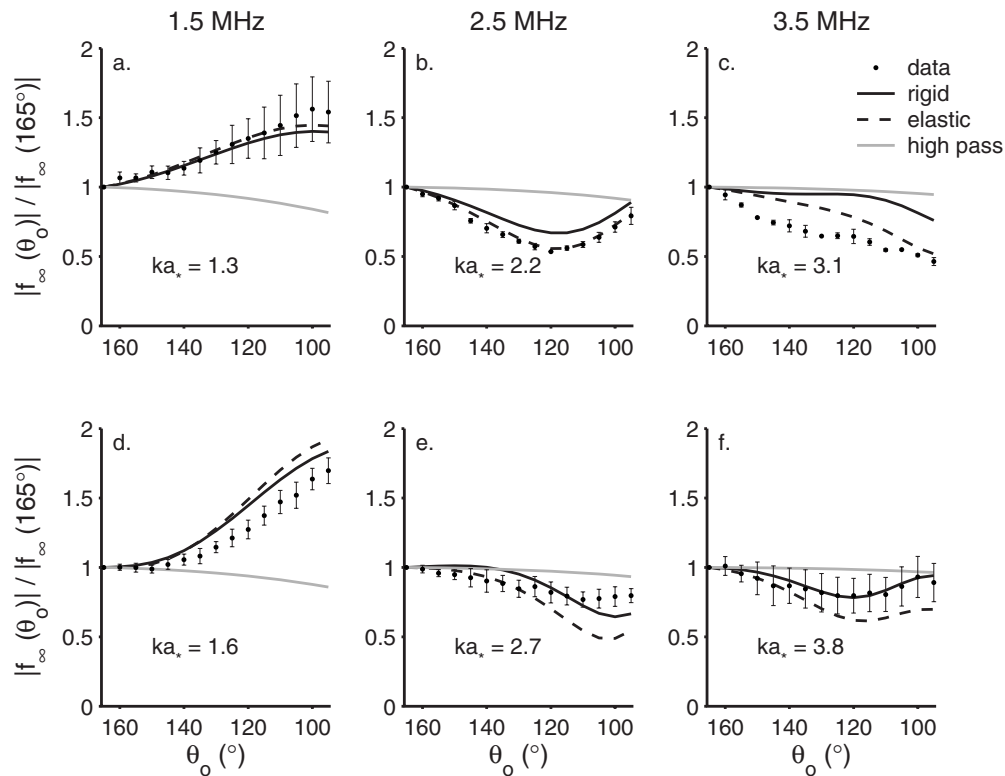


FIG. 8. Measured and predicted scattered amplitudes at three frequencies for suspensions of [(a)–(c)] large lead-glass beads and [(d)–(f)] large sand, normalized to $\theta_0=165^\circ$. The error bars represent \pm the standard error (i.e., the standard deviation divided by $\sqrt{2}$, for three repeat experiments). The equivalent plots for the small particles are presented and discussed in Appendix B.

For a plane-wave incident on a sphere, the diffraction pattern is due to interference between the incident wave field and energy leaked by creeping waves traveling along geodesics on the surface of the sphere.^{24–26} For an irregularly shaped particle, the creeping wave circuits will not be of equal length, and the constant phase relationships required for interference will be disrupted. Thus, as with the lack of resonant features in backscattering and total scattering cross section measurements for sand at higher values of ka ,^{3,4,16} the diffraction pattern for a suspension of randomly-oriented sand grains should be a blurred version of that for a smooth sphere. To mimic the smearing effect, we tried smoothing the best-fit predictions along the θ -axis using a Gaussian weighting function with a standard deviation of 5° . For the smearing mechanism to be consistent, smoothing the theory in this way should lead to improved agreement, and indeed does. For large sand, the smoothed theory led to a reduction in γ^2 from 0.30 to 0.21.

B. Effective particle size

Thorne and Buckingham⁴ showed that measurements of the backscattering and total scattering cross sections for sand in aqueous suspensions can be collapsed onto smoothed versions of the predictions for a sphere, using non-linear scaling with a single free parameter. However, the value of the scaling parameter differed among the available data sets, and varied systematically with particle size (by almost a factor of 2) for some of the total scattering cross section measurements.

In principle, there are two independent particle size scales involved when comparing measurements of scattering from particulate suspensions with narrow size distributions to spherical scatterer theory. One scale is the circumference of an equivalent sphere to scale the wavelength, yielding ka for the scattering computations. The second scale is the diameter of the equal volume sphere for converting particle mass concentration, M , to particle number density, N : that is, $\rho_s N = M/v_p$, where ρ_s is the grain density and v_p is the particle volume. M is measured (gravimetrically here, using the suction samples), but N is required in the theory [see Eq. (1)]. For irregularly shaped scatterers, there is no reason to expect, *a priori*, that the two scales should be the same.

Schaafsma and Hay³ found that measurements of acoustic attenuation in aqueous suspensions of natural sand could be brought into agreement with rigid sphere theory using a two-parameter approach. Their scaling is linear: that is, the scaled diameter is given by Bd , where d is the measured diameter and B is one of the parameters. The values obtained for the wavelength scaling parameter were relatively constant. In contrast, the volume scaling parameter varied with mean size in a manner consistent with the fact that the particles tended to be less rounded and more angular with decreasing size. It is convenient here to designate the two parameters as B_λ and B_N , the subscripts denoting their respective physical roles.

Because normalizing the scattered amplitudes eliminates the dependence on scatterer concentration [see Eq. (2)], the results presented here should depend on B_λ only. Thus, it is interesting that the ratio of best-fit acoustic size to measured

mean size, i.e., B_λ , is within 4% of unity for the Coulter Counter measured mean sizes (Table III). Since the Coulter Counter method yields a volume equivalent size, and since B_N should be identical to unity for volume-based size measurements, an implication is that the two linear scaling parameters could be reduced to one when the measured size is based on particle volume, at least for the ka range of the present data, and for sand grains of comparable sphericity.

For the unsieved sand, the best-fit acoustic size differed from the measured median diameter by only 6% (Table III), but the measured size in this case was obtained by sieving. Given the greater breadth of the size distribution for the unsieved sand, this result might suggest that, for the broader distributions more likely to be encountered in natural environments, sieve size could be used instead of Coulter Counter size. However, as particle volume is proportional to d^3 , an error of 5%–10% in size would lead to an error of 15%–30% in number density N , which might not be acceptable.

VI. SUMMARY AND CONCLUSIONS

The angular dependence of sound scattering from particles suspended in a turbulent jet has been investigated. The measurements were made from 1.5 to 4.0 MHz with 125 kHz resolution, at scattering angles ranging from 95° to 165°, for suspensions of both nominally spherical lead-glass beads and natural sand. Two narrow size fractions for each of the beads and sand were used: one with a nominal mean diameter of $\sim 200 \mu\text{m}$ and the other, $\sim 500 \mu\text{m}$. Particle size was determined by Coulter Counter for both particle types. Optical image analysis was used to quantify the irregularity of the sand grain shapes. While the transparency of lead-glass precluded the use of the image analysis method for the beads, their shapes had been examined previously by scanning electron microscopy.³ The size distributions were nominally Gaussian for all particles, and especially so for the small and large sand size fractions. The sphericity of the sand grains, defined as the ratio of projected perimeter size to projected area size, was 1.08 ± 0.03 . The scattering measurements were made at non-dimensional wavenumbers of $0.7 \leq ka_* \leq 1.8$ for the small lead-glass beads and $1.3 \leq ka_* \leq 3.5$ for the large beads, and at $0.7 \leq ka_* \leq 1.8$ and at $1.6 \leq ka_* \leq 4.4$ for the small and large sand size fractions respectively.

Theoretical angular scattering patterns were computed for both rigid movable and elastic movable spheres assuming Gaussian size distributions with the same breadth-to-mean diameter ratios as the measured distributions. Effective acoustic mean diameters were determined by least-squares fitting the experimental results to the predicted scattering patterns, resulting in an overall best-fit mean diameter (d_*) and overall best-fit model (rigid or elastic) for each scatterer type and size fraction. Consistent with previous measurements of the backscattering and total scattering cross sections for glass bead and natural sand particles in suspension, the elastic sphere model provided the best fit to the lead-

glass bead data; the rigid sphere model provided the best fit for sand. The modified high-pass model² does not fit the data, except at the smallest values of ka .

For each particle type and each size fraction, the best-fit mean diameter was very close to the Coulter Counter value: within 1% for the lead-glass beads and within 4% for the sand. Since the possible error in the Coulter Counter measurements is a few percent at least,^{21,27} these values are probably not significantly different from zero. Since particle size measured by the Coulter Counter should be close to the diameter of a sphere of equal volume, the results for the nominally spherical lead-glass beads are expected. The results for sand indicate that the diameter of an equal volume sphere can be used to scale the acoustic wavenumber, at least over the ka range of the present measurements and for sand grains with sphericity comparable to the sand used here. This result has potential implications for inverting acoustic scattering data to suspended sand size and concentration.

The lead-glass bead data are in better agreement with the elastic sphere model than are the sand data with the predictions for a rigid sphere. Since the measurements were made at ka values below the resonances for quartz spheres, but well above the Rayleigh range, the departures from spherical scatterer theory for sand must be related to diffraction and must involve sand grain shape. The authors conclude that the irregular shapes of natural sand grains partially disrupt the creeping wave interferences responsible for the diffraction pattern for a smooth sphere. As a result, the diffraction-induced undulations in the scattering pattern are smoother than predicted by spherical scatterer theory. One implication of this result is that it provides justification for smoothing the scattering cross sections predicted by spherical scatterer theory in the so-called diffraction region of ka -space, even for suspensions of sand grains with very narrow size distributions.

ACKNOWLEDGMENTS

We thank Wesley Paul and Robert Craig for technical support, and Brent Law and Tim Milligan for the Coulter Counter measurements. This project was supported by the Natural Sciences and Engineering Research Council of Canada.

APPENDIX A: BISTATIC SCATTERING FROM ISOTROPIC, FREQUENCY-INDEPENDENT SCATTERERS IN THE JET

The purposes of this Appendix are (1) to verify that the change in detected volume with scattering angle is small, an assumption made in obtaining Eq. (2); and (2) to explain the change in apparent jet width with scattering angle indicated in Fig. 2. To do so, the angular dependence of scattering from the jet is investigated assuming the scattering cross section to be independent of frequency and scattering angle. The predicted variations with scattering angle will thus be entirely due to geometric effects, and the sole source of frequency variation will be the transducer beam patterns. The coordinate system is sketched in Fig. 9. The axis of the jet is

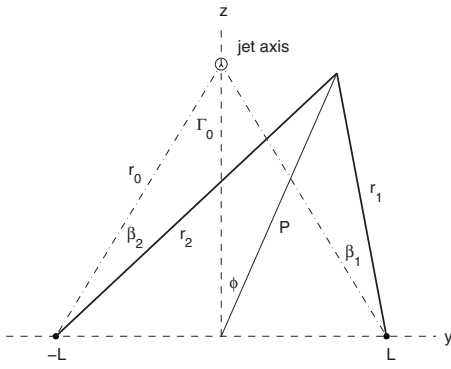


FIG. 9. Sketch of bistatic scattering geometry. The transducers are located at $y = \pm L$. The x -axis (not shown) is out of the page and anti-parallel to the axis of the jet (indicated by the circle).

anti-parallel to the positive x -axis, and the origin is the midpoint between the two transducers, each located at $y = \pm L$ in the $x=0$ plane.

Scattered signals from different particles arrive at the receiver at the same time (i.e., within a wave period) if

$$r_1 + r_2 = 2r_0 \quad (\text{A1})$$

This relation defines an ellipsoidal surface centered on the origin with its axis of symmetry coincident with the y -axis. Consider any field point with position vector $\mathbf{P} = x\hat{i} + y\hat{j} + z\hat{k}$ that satisfies Eq. (A1). In spherical polar coordinates, $x = P \sin \phi \cos \varphi$, $y = P \sin \phi \sin \varphi$, and $z = P \cos \phi$, ϕ being the polar angle and φ the azimuthal angle. Thus, $\mathbf{r}_1 = \mathbf{P} - \mathbf{L}$ and $\mathbf{r}_2 = \mathbf{P} + \mathbf{L}$, where $\mathbf{L} = L\hat{j}$. It follows that

$$r_2^2 - r_1^2 = 4Ly, \quad (\text{A2})$$

and

$$P = \left[\frac{r_1^2 + r_2^2}{2} - L^2 \right]^{1/2} \quad (\text{A3})$$

Equations (A1) and (A2) yield

$$r_1 = r_0 - \frac{L}{r_0}y \quad (\text{A4})$$

and

$$r_2 = r_0 + \frac{L}{r_0}y. \quad (\text{A5})$$

Using the relation $\mathbf{r}_0 \cdot \mathbf{r} = r_0 r \cos \beta$, the angle of the field point relative to the acoustic axis of the transducer at $y=L$ is given by

$$\cos \beta_1 = \frac{r_0 z \cos \Gamma_0 - L(y - L)}{[x^2 + (y - L)^2 + z^2]^{1/2} [L^2 + r_0^2 \cos^2 \Gamma_0]^{1/2}} \quad (\text{A6})$$

and that relative to the axis of the transducer at $y=-L$ by

$$\cos \beta_2 = \frac{r_0 z \cos \Gamma_0 + L(y + L)}{[x^2 + (y + L)^2 + z^2]^{1/2} [L^2 + r_0^2 \cos^2 \Gamma_0]^{1/2}}, \quad (\text{A7})$$

where $2\Gamma_0$ is the angle subtended at the jet centerline by the transducer baseline, and is related to the scattering angle θ_0 by $2\Gamma_0 = \pi - \theta_0$.

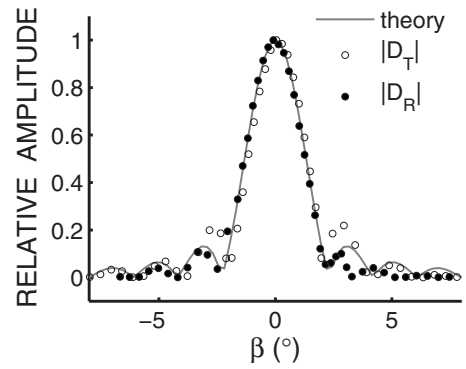


FIG. 10. Measured transducer directivity at 2.9 MHz for the transmit, D_T , and receive, D_R , transducers compared to Eq. (A11) ($a_0=0.75$ cm). β is the angle of the field point relative to the acoustic axis (see Fig. 9).

The radial distance to the field point from the jet centerline is

$$\rho = [y^2 + (z - r_0 \cos \Gamma_0)^2]^{1/2}. \quad (\text{A8})$$

Let σ_{J0} be the jet standard deviation at $x=0$ and x_* the distance from the nozzle to the plane of the transducers. Then $\sigma_J = \sigma_{J0}(x_* - x)/x_*$ accounts for the linear spreading of the jet with downstream distance, and

$$N(x, y, z) = \frac{x_* N_0}{x_* - x} \exp[\rho^2 / 2\sigma_J^2] \quad (\text{A9})$$

is the number density of scatterers. N decays hyperbolically with distance from the nozzle, as required for round jets.

For omnidirectional scatterers with scattering cross sections independent of frequency, the mean-squared scattered pressure is then proportional to

$$\iint \frac{D_1^2(\beta_1) D_2^2(\beta_2)}{r_1^2 r_2^2} NP^2 \sin \phi d\phi d\varphi, \quad (\text{A10})$$

where $D(\beta)$ is the transducer directivity. The theoretical directivity for a circular piston transducer is given by²⁸

$$D(\beta) = 2J_1(ka_0 \sin \beta) / ka_0 \sin \beta, \quad (\text{A11})$$

J_1 being a cylindrical Bessel function. Figure 10 shows the measured beam patterns for both transducers compared to Eq. (A11). The measurements were made using a standard target located at the jet axis, by rotating one transducer about a vertical axis while the other remained fixed. The standard target was a 1 m long, 0.236 mm diameter stainless steel rod, suspended vertically below the nozzle. Scattering of spherical waves by long cylinders and their use as standard targets has been discussed elsewhere.^{29,30} In the figure, the comparison between theory and experiment is quite good, although the value of 0.75 cm used for a_0 in the calculation is 15% larger than the manufacturer's specified radius for the active element in the transducer. Based on Eq. (A11) with $a_0 = 0.75$ cm, the full width at half maximum (FWHM) of D^2 , i.e., the beamwidth of one transducer, is 2° , and of $D_1^2 D_2^2$ is 1.4° . This angular FWHM corresponds to an arc length of 1.1 cm at 45 cm range, which is much less than the 6 cm ($2\sigma_{J0}$) characteristic width of the jet (see Fig. 1).

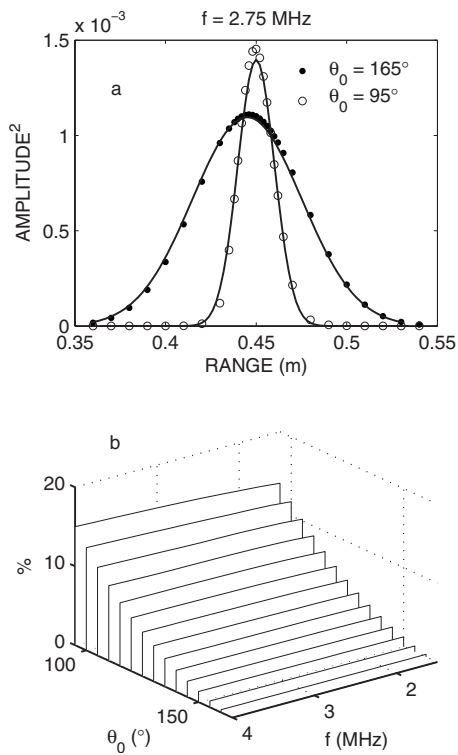


FIG. 11. (a) Theoretical profiles of mean-square scattered signal level at scattering angles of 95° and 165° assuming isotropic, frequency-independent scatterers suspended in the jet. Points are the predictions from Eq. (A10) with $\sigma_{j0}=3$ cm in Eq. (A9). Solid curves are the Gaussian fits to these points, after convolution with a constant-amplitude transmit pulse of length $c\tau/2=1.2$ cm. (b) Theoretical scattering pattern for isotropic, frequency-independent scatterers in the jet, normalized by the values at $\theta_0=165^\circ$.

The resulting theoretical profiles of the mean square scattered signal levels from Eq. (A10) are plotted in Fig. 11(a) for scattering angles of 165° and 95° . D was computed using Eq. (A11) with $a_0=0.75$ cm. The integration was carried out for values of x and y ranging between $\pm 3\sigma_{j0}$. The solid lines are the Gaussian fits to the predicted points, after convolution with a boxcar function of length equal to the 1.2 cm pulse length (i.e., $c\tau/2$, τ being the $16 \mu\text{s}$ pulse duration). The pulse length is short enough that the convolution has a noticeable effect only for the narrow profile at 95° . Comparing Fig. 11(a) with Fig. 2, the predicted reduction in apparent jet width with decreasing scattering angle (from 3.0 to 0.97 cm) is nearly identical to that observed (from 3.1 cm to 0.96 cm). As indicated earlier, this reduction in apparent width is due physically to the reduced overlap area between the transmit and receive beams as the scattering angle approaches 90° .

Figure 11(b) shows the scattering pattern obtained using Eq. (A10), normalized by the values at $\theta_0=165^\circ$. Rather than a scattering amplitude independent of scattering angle, as would be expected for isotropic scatterers, the theory predicts a geometry-induced bias in the observed scattering patterns. The value of γ^2 represented by the bias is 0.0049, small compared to those in Table IV. Because the bias is relatively small ($\leq 15\%$), no correction has been applied to the data.

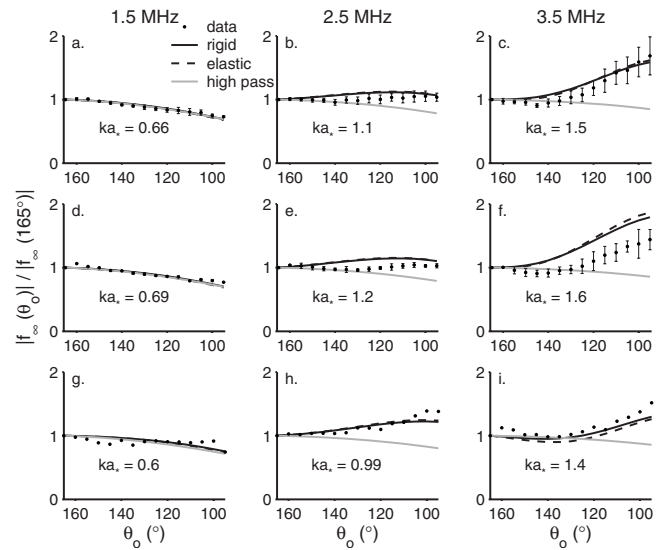


FIG. 12. Measured and predicted scattered amplitudes at three frequencies for suspensions of [(a)–(c)] small lead-glass beads, [(d)–(f)] small sieved sand, and [(g)–(i)] small unsieved sand, normalized to $\theta_0=165^\circ$. Error bars indicate \pm the standard error for the small lead-glass beads and small sieved sand. Only one experiment was run with the unsieved sand, so no error estimates are available for this case.

Finally, the scattering angle clearly changes with position in the jet. This variation, $\Delta\theta_0$, was computed using the above equations for $r_1+r_2=90$ cm: i.e., for the ellipsoidal surface tangent to the jet centerline. For points with $10 \log(D_1^2 D_2^2) > -6$ dB, the computed values of $\Delta\theta_0$ were 0.1° or less for all measured frequencies and scattering angles. Thus, departures from θ_0 due to the finite size of the detected volume should have been negligible.

APPENDIX B: SMALL SCATTERERS REVISITED

The plots equivalent to those in Fig. 8, but for the $\sim 200 \mu\text{m}$ diameter particles, are shown in Fig. 12. There are three main points to note about Fig. 12 in comparison to Fig. 8.

The first is that there is very little difference between the predictions of the elastic and rigid models. This is expected because, for $ka_* \leq 1.6$, the scattered amplitude is dominated by the $n=0$ and $n=1$ partial waves, and the amplitudes of these waves are relatively insensitive to the shear wave speed, at least for particles with the density of quartz or lead-glass suspended in water.

The second point to note is that the modified high-pass model, while agreeing with the data at low frequencies, provides progressively worse agreement as frequency increases. The good agreement at 1.5 MHz is expected, since $ka_* < 1$, and the modified high-pass model is exact in the Rayleigh region. The relatively poor agreement with the high-pass model at 3.5 MHz is consistent with the results for the large particles in Fig. 8.

The third point of note is the relatively good agreement between the data and spherical scatterer theory in eight of the nine panels. The exception is panel f, the small sand at 3.5 MHz: the elastic and/or rigid models exhibit trends similar to the data, but the data are systematically lower. This

disagreement is consistent with the best-fit value of γ^2 being larger for the small sand (Fig. 7). In contrast, the unsieved small sand agrees comparatively well with the model predictions, suggesting that spherical scatter theory ought to provide a good fit to the small sieved sand data. In addition, much better agreement between theory and experiment is exhibited by the large sand data at the same value of ka_* [Fig. 8(d)]. Thus, the only explanation the authors have for the relatively poor quantitative agreement between theory and the sieved small sand data is that these data are in error, but we have been unable as yet to identify the cause.

- ¹P. D. Thorne and D. M. Hanes, "A review of acoustic measurement of small-scale sediment processes," *Cont. Shelf Res.* **22**, 603–632 (2002).
- ²J. Sheng and A. E. Hay, "An examination of the spherical scatterer approximation in aqueous suspensions of sand," *J. Acoust. Soc. Am.* **83**, 598–610 (1988).
- ³A. S. Schaafsma and A. E. Hay, "Attenuation in suspensions of irregularly shaped sediment particles: A two-parameter equivalent spherical scatterer model," *J. Acoust. Soc. Am.* **102**, 1485–1502 (1997).
- ⁴P. D. Thorne and M. J. Buckingham, "Measurements of scattering by suspensions of irregularly shaped sand particles and comparison with a single parameter modified sphere model," *J. Acoust. Soc. Am.* **116**, 2876–2889 (2004).
- ⁵V. K. Varadan, Y. Ma, and V. V. Varadan, "Scattering and attenuation of elastic waves in random media," *Pure Appl. Geophys.* **131**, 577–603 (1989).
- ⁶J. Ribberink, "Bed-load transport for steady flows and unsteady oscillatory flows," *Coastal Eng.* **34**, 59–82 (1998).
- ⁷A. E. Hay and D. G. Mercer, "On the theory of sound scattering and viscous absorption in aqueous suspensions at medium and short wavelengths," *J. Acoust. Soc. Am.* **78**, 1761–1771 (1985).
- ⁸P. M. Morse and K. U. Ingard, *Theoretical Acoustics* (McGraw-Hill Book, New York, 1968), p. 927.
- ⁹Lord Rayleigh, *Theory of Sound*, 2nd ed. (Dover, New York, 1945), Vol. 2, p. 504.
- ¹⁰J. J. Faran, "Sound scattering by solid cylinders and spheres," *J. Acoust. Soc. Am.* **23**, 405–418 (1951).
- ¹¹A. E. Hay and R. W. Burling, "On sound scattering and attenuation in suspensions, with marine applications," *J. Acoust. Soc. Am.* **72**, 950–959 (1982).
- ¹²R. Hickling, "Analysis of echoes from a solid elastic sphere in water," *J. Acoust. Soc. Am.* **34**, 1582–1592 (1962).
- ¹³K. G. Foote, "Optimizing copper spheres for precision calibration of hydroacoustic equipment," *J. Acoust. Soc. Am.* **71**, 742–747 (1982).
- ¹⁴A. E. Hay and A. S. Schaafsma, "Resonance scattering in suspensions," *J. Acoust. Soc. Am.* **85**, 1124–1138 (1989).
- ¹⁵G. Batchelor, *An Introduction to Fluid Dynamics* (Cambridge University Press, New York, 1967), p. 615.
- ¹⁶A. E. Hay, "Sound scattering from a particle-laden, turbulent jet," *J. Acoust. Soc. Am.* **90**, 2055–2074 (1991).
- ¹⁷S. A. Moore, "The angular dependence of acoustic scattering from suspended sediment," MS thesis, Dalhousie University (2008), Nova Scotia, Canada.
- ¹⁸H. B. Fischer, E. J. List, R. C. Koh, J. Imberger, and N. H. Brooks, *Mixing in Coastal and Inland Waters* (Academic, New York, 1979), p. 472.
- ¹⁹V. V. Kharin and F. W. Zwiers, "Climate predictions with multimodel ensembles," *J. Clim.* **15**, 793–799 (2002).
- ²⁰R. L. Ingram, "Sieve analysis," in *Procedures in Sedimentary Petrology*, edited by R. E. Carver (Wiley-Interscience, Toronto, 1971).
- ²¹T. Allen, *Powder Sampling and Particle Size Determination* (Elsevier, New York, 2003), p. 627.
- ²²J. P. M. Syvitski, K. W. G. LeBlanc, and K. W. Asprey, "Interlaboratory, interinstrument calibration experiment," in *Principles, Methods, and Application of Particle Size Analysis*, edited by J. P. M. Syvitski (Cambridge University Press, Cambridge, 1991), pp. 174–193.
- ²³R. K. Johnson, "Sound scattering from a fluid sphere revisited," *J. Acoust. Soc. Am.* **61**, 375–377 (1977).
- ²⁴W. Franz and K. Deppermann, "Theorie der beugung am zylinder unter berücksichtigung der kriechwelle (Theory of diffraction by a cylinder accounting for creeping waves)," *Ann. Phys.* **445**, 361–373 (1952).
- ²⁵W. G. Neubauer, "Observation of acoustic radiation from plane and curved surfaces," in *Physical Acoustics*, edited by W. P. Mason and R. N. Thurston, (Academic, New York, 1973), Vol. **10**, pp. 174–193.
- ²⁶H. Überall, "Surface waves in acoustics," in *Physical Acoustics*, edited by W. P. Mason and R. N. Thurston (Academic, New York, 1973), Vol. **10**, pp. 1–60.
- ²⁷I. N. McCave and J. P. M. Syvitski, "Principles and methods of geological particle size analysis," in *Principles, Methods, and Application of Particle Size Analysis*, edited by J. P. M. Syvitski (Cambridge University Press, Cambridge, 1991), pp. 174–193.
- ²⁸C. S. Clay and H. Medwin, *Acoustical Oceanography: Principles and Applications* (Wiley-Interscience, Toronto, 1977).
- ²⁹D. T. DiPerna and T. K. Stanton, "Fresnel zone effects in the scattering of sound by cylinders of various lengths," *J. Acoust. Soc. Am.* **90**, 3348–3355 (1991).
- ³⁰J. Sheng and A. E. Hay, "Spherical wave backscatter from straight cylinders: Thin-wire standard targets," *J. Acoust. Soc. Am.* **94**, 2756–2765 (1993).